The Apparent Stratification at the Top of Earth's Liquid Core

Jon Mound*[1], Chris Davies[1], Sebastian Rost[1] & Jon Aurnou[2]

[1]*School of Earth and Environment, University of Leeds, Leeds LS2 9JT, UK*

[2]*Department of Earth and Space Sciences, University of California, Los Angeles, California 90095-1567, USA.*

A stably stratified layer at the top of Earth's liquid core has been independently inferred from seismology[1–3], geomagnetism[4], and geodynamics[5,6], contradicting the classic view of a thermally and chemically well-mixed core. Such a layer would have significant implications for the dynamics and evolution of the core and the power available to generate the geomagnetic field. Previous models have attempted to explain observations of anomalously slow seismic wave speeds, that may extend up to ~ 350 km below the core-mantle boundary (CMB)[3], with a global stably stratified layer resulting from diffusive processes[7–9]. However, geomagnetic features such as high-latitude flux patches and reversed flux in the Atlantic[10] are often associated with radial flow near the CMB[11] and thus appear incompatible with a thick global stable layer. Here we propose that both geomagnetic and seismic observations can be reconciled within a framework of regional thermal inversion at the top of the core due to imposed lateral variations in CMB heat flow. These regional thermal inversion layers are expected under anomalously hot regions of the lowermost mantle, can extend 100's of kilometres into the core and, if sufficiently large and strong, can result in a 1D temperature profile that could

be mistaken for the existence of a density stratified global layer below the CMB. However, dynamic links between regions of thermal inversion and active convection result in radial motion everywhere within the core, thereby avoiding any conflict with geomagnetic observations associated with such motions.

While there is little doubt that the bulk of Earth's liquid core is undergoing turbulent convection, the possible existence of a stably stratified layer below the CMB has been vigorously debated. Several studies[1–3] have found that seismic wave speeds in the top few hundred kilometres of the core depart from those expected for a well-mixed and adiabatic fluid, although other studies find no such evidence[12]. A vigorously convecting core is expected to be laterally uniform[13] and a dynamically stable layer at the top of the core would need to be anomalously buoyant. Therefore, despite unavoidable limitations in the geographic coverage of seismic data, anomalous seismic wave speeds have been interpreted as a global stably stratified layer. Such a layer would allow a range of wave dynamics not found in a fully convecting core[14] and these waves have been invoked to explain certain periodic variations of the geomagnetic field[4], though this explanation is not unique. Models of core flow inverted from the observed geomagnetic secular variation suggest minimal radial flow just below the CMB, consistent with a global stratification; however, stronger radial motions cannot be excluded[15]. Indeed, concentrated patches of magnetic flux at high latitudes and in the southern Atlantic[10] are hard to explain without invoking radial motion[11], perhaps within ~ 100 km of the CMB[16].

Three principle mechanisms have been invoked to explain the existence of a globally stable layer. The first suggests that the core has slowly cooled to a point where the heat flux, q, has fallen below the adiabatic heat flux, q_{a}, across the CMB[7]. This scenario produces a wide range of thickness estimates[17] that rely on the poorly-known CMB heat flow and much-debated core conductivity[6]. The second mechanism invokes chemical diffusion, either along the core pressure gradient[9] or across the CMB from the mantle[8], which enriches the top of the core in light elements; however, predicted layer thicknesses are limited to the diffusion scale, $O(100)$ km. The third possibility is emplacement of a light layer during core formation[18], which must then avoid disruption throughout the lifetime of the Earth or by the moon-forming impact[19]. All of these scenarios are motivated by the idea that a global layer at the top of the core is required to explain departures from the presumed well-mixed adiabatic state.

We propose an alternative scenario wherein regional non-adiabatic structure near the top of the core is induced by the lateral variations in CMB heat flux that are an inevitable consequence of thermochemical heterogeneity in the lowermost mantle[20]. Although the bulk of the core remains vigorously convecting and adiabatically well mixed, sufficiently hot regions in the lowermost mantle can reduce q below q_{a} preventing thermally driven convection and allowing regional accumulations of hot fluid at the top of the core. Rather than the traditional view of a laterally homogeneous globally stratified layer, we predict large lateral variations between adiabatic regions undergoing vigorous convection and more stagnant regions of thermal inversion.

We investigate this scenario using a numerical model of non-magnetic rotating convection that includes two patterns and two amplitudes, $q^{\star}$, of CMB heat flux heterogeneity (see methods and our previous work[21]). Our suite of 112 simulations push towards the rapidly-rotating, highly turbulent regime relevant to the Earth's core by considering higher Rayleigh numbers ($\widetilde{Ra}$) and lower Ekman numbers (E) than previous models that incorporate CMB heat flux heterogeneity[22–24]. We find that convectively-stable regions of thermal inversion ($\mathrm{d}T/\mathrm{d}r > 0$) can be maintained over large lateral and radial extents (figure 1, supplementary figure 1), although the bulk of the core remains strongly convecting and hence well mixed on short length scales. Even in regions where the CMB heat flux remains superadiabatic an inversion layer can exist a few hundred kilometres below the CMB as azimuthal flow sweeps hot material horizontally. The lateral and depth extents of the regional inversion layers are associated with the long wavelengths of the imposed boundary heterogeneity rather than the small wavelengths of the convecting core. Indeed the small scales of the convective fluctuations may inhibit their ability to disrupt the large regions of thermal inversion; previous studies at low $\widetilde{Ra}$ did not find the stratification signal[22], perhaps because the potentially stable regions were disrupted by the large scale convective patterns close to onset. If the regional inversion layers are sufficiently large and strong, the horizontally-averaged temperature gradient near the top of the core can become positive (supplementary figures 2, 3, 4), an apparent global stratification despite the average heat flux across the CMB being strongly superadiabatic. As $\widetilde{Ra}$ is increased, the bulk of the core becomes more isothermal and the horizontally averaged temperature gradient near the top of the core is increasingly dominated by the large gradients that exist in the regional inversion layers.

We calculate the regional inversion layer thickness by determining the depth range for which the time-averaged temperature gradient is positive at $\theta = \pi/2, \phi = 0$ ('Africa') and $\theta = \pi/2, \phi = \pi$

(Pacific) (figures 2, 3). The thickness decreases with decreasing Ekman number and increases with increasing $q^\star$. The scaling of layer thickness as a function of $\widetilde{Ra}$ changes depending on the chosen E, $q^\star$, and boundary heterogeneity pattern (figure 2, upper panels). The strength of the inversion is determined by the maximum Brunt-Väisälä frequency, N, which we normalise relative to 2Ω (twice the planetary rotation rate). We expect the strength of the inversion to scale as

$$\left.\frac{N}{2\Omega}\right|_{\max} \approx \left(\frac{1}{r_{\mathrm{o}}^\star}\right)\sqrt{\frac{\widetilde{Ra}E}{Pr}\left(\frac{q^\star-2}{2}\right)}, \tag{1}$$

where Pr is the Prandtl number and $r_{\mathrm{o}}^\star$ is the dimensionless CMB radius (see methods). For the stratified regions beneath the Pacific and Africa in our simulations the Brunt-Väisälä frequency decreases as the Ekman number is lowered (figure 2, lower panels), whereas it increases with Rayleigh number at fixed E. Stronger boundary heterogeneity (larger $q^\star$) implies more anomalous $\mathrm{d}T/\mathrm{d}r$ at the CMB and thus N also increases with $q^\star$. Overall, strong and thick regional inversion layers are ubiquitous within our simulations.

Although our simulations reach the geophysically relevant regime of strong driving and rapid rotation rates, Earth-like values of the control parameters remain computationally inaccessible (see methods). Direct extrapolation of our result to Earth's core is hampered by the complex parameter dependencies discussed above. Regardless, mantle heterogeneity is sufficiently strong that large areas of the CMB are expected to have a subadiabatic heat flux[25]. Such regions will inevitably inhibit convection over extended regions of the outermost liquid core resulting in the development of regional inversion layers. The lateral extent of these regions is set by the wavelength of the boundary heterogeneity, rather than that of the small scale convection, therefore the broad and thick layers seen in our simulations are also expected for the Earth. Unlike our Boussinesq numerical model, the anomalous regions in Earth's core need not have a strict thermal inversion, they need only have a sub-adiabatic temperature gradient to be dynamically distinct from the bulk of the core.

The lateral temperature differences expected[13,26] within convecting regions of the outer core are very small, $O(10^{-4})$ K; however, the temperature difference between these regions and the top of the regional inversion layers can be far larger, reaching 10's or 100's of kelvin (see methods, supplementary figure 5). Convection in Earth's core arises due to the release of both chemical and thermal buoyancy as the core cools and the inner core solidifies. Positive correlation between the temperature and compositional fields is expected[24] and would result in the thermal inversion layers also being chemically distinct from the actively convecting region. The impact of these large thermo-chemical variations on seismic wave speeds would be similar to those associated with previous mechanisms of stable layer formation[7,9,18] but would allow lateral as well as radial variation. However, such regional variations have not been considered by seismological studies; published results and their related error bounds currently do not allow us to differentiate between regional and global models of outer core velocity structure (see methods).

Although radial motion would be inhibited within a strongly stratified global layer, the regions of temperature inversion in our simulations are dynamically connected to the rest of the core and thus radial velocity is not completely suppressed within them (figure 4). The lateral variations in CMB heat flux drive thermal winds that can sweep material near the top of these regions into the well-mixed, vigorously convecting bulk and result in a broad, weak upwelling through the regional inversion layers. Unlike previous studies that consider subadiabatic, or weakly superadiabatic, heat flux at the CMB[7,17,24,27] all of the simulations we consider here are strongly supercritical ($\widetilde{Ra} \geq 10\widetilde{Ra}_{\mathrm{crit}}$), even those for which the top of the core has a net thermal inversion. Thermal stratification at the top of the core in our simulations is only apparent; the bulk of the core is vigorously convecting and the regional inversion layers are not stagnant. As a result, there is no difficulty in reconciling this scenario with both geomagnetic observations that suggest upwelling near the CMB[16] and seismic observations of a relatively thick anomalous layer[2].

Regional inversion layers will have a different impact on geomagnetic or seismic observations than a uniform stratified layer providing observational tests of this scenario. Seismic studies of the outermost liquid core generally assume a uniform global structure; however, the scenario we propose would allow for lateral variations in seismic velocity at the top of the core much larger than previously suspected. The regional inversion layers should be most prominent in equatorial regions and particularly under the Pacific and Africa Large Low Velocity Provinces (LLVP's). Magneto-hydrodynamic waves at the top of the core would behave differently in the presence of these large regional inversion layers, compared to a simple 1D radial structure, and if such waves make a substantial contribution to secular variation, then regional variations in secular variation would be expected. Regardless of the impact of waves on secular variation, the fluid flow in inversion layers is different to that in the bulk of the core (figure 4), which would result in different geomagnetic variation. Hemispheric patterns in geomagnetic secular variation[28] may suggest that only one dominant regional core inversion layer is present. The latitudinal and longitudinal extents of the two LLVP's are quite different, which could result in differing influences on core thermal structure, and hence geomagnetic variation induced by flow or waves. A hemispheric difference could also arise due to differences in temperature between the Pacific and African LLVP's, which might reflect differing balances between thermal and chemical contributions to these LLVP's origins.

Methods

Governing equations. We employ a numerical model of non-magnetic rotating convection of a homogeneous Boussinesq fluid confined within a rotating spherical shell[29], with fixed-flux thermal boundary conditions and no slip velocity boundary conditions. In non-dimensional form the conservation equations for momentum, energy, and mass are

$$\frac{E}{Pr}\left(\frac{\partial \boldsymbol{u}}{\partial t} + (\boldsymbol{u}\cdot\boldsymbol{\nabla})\,\boldsymbol{u}\right) + \hat{\boldsymbol{z}}\times\boldsymbol{u} = -\boldsymbol{\nabla}P + \widetilde{Ra}T'\boldsymbol{r} + E\nabla^2\boldsymbol{u}, \tag{2}$$

$$\frac{\partial T}{\partial t} + (\boldsymbol{u}\cdot\boldsymbol{\nabla})\,T = \nabla^2 T, \tag{3}$$

$$\boldsymbol{\nabla}\cdot\boldsymbol{u} = 0, \tag{4}$$

where $\boldsymbol{u}$ and T are the velocity and temperature fields, respectively, and T' are the temperature fluctuations relative to the steady-state temperature profile in the absence of flow. The pressure term, P, includes the centrifugal potential. The fluid is characterised by its constant thermal expansion, α, thermal diffusivity, κ, kinematic viscosity, ν, and reference density, ρ_0. The fluid shell is defined by its inner and outer boundaries, r_i and r_o, respectively, and rotates with a constant angular velocity $\boldsymbol{\Omega} = \Omega\hat{\boldsymbol{z}}$. Gravity varies with radius according to $\boldsymbol{g} = -(g_\mathrm{o}/r_\mathrm{o})\boldsymbol{r}$. We have non-dimensionalised using the shell thickness $L = r_\mathrm{o} - r_\mathrm{i}$ for the length scale, the thermal diffusion time $\tau = L^2/\kappa$ for the time scale, and β/L for the temperature scale, where $\beta = Q/4\pi k$, Q is the total heat flow through the outer boundary, $k = \kappa\rho_0 C_p$ is the thermal conductivity and C_p the heat capacity of the fluid. The resulting control parameters are the Prandtl number $Pr = \frac{\nu}{\kappa}$, Ekman number $E = \frac{\nu}{2\Omega L^2}$, and modified Rayleigh number $\widetilde{Ra} = \frac{\alpha g_o \beta}{2\Omega\kappa}$.

Control parameters for the present study. The amplitude of CMB heat flux heterogeneity in our numerical model is described by $q^\star = \frac{q_{\mathrm{max}} - q_{\mathrm{min}}}{q_{\mathrm{ave}}}$, where q_{max}, q_{min}, and q_{ave} are the maximum, minimum and horizontally averaged heat fluxes through the outer boundary, respectively. Our previous study[21] includes a suite of 106 simulations with values of $q^\star = \{0.0, 2.3, 5.0\}$, $Pr = 1$, $E = \{10^{-4}, 10^{-5}, 10^{-6}\}$, and $\widetilde{Ra}$ up to ~ 800 times the critical value for the onset of convection $\widetilde{Ra}_{\mathrm{crit}}$. In this work we restrict our attention to simulations for which $\widetilde{Ra} \geq 10\widetilde{Ra}_{\mathrm{crit}}$ to ensure that we have left the weakly non-linear regime near the onset of convection. The critical Rayleigh number increases as the Ekman number is reduced and has values of $\widetilde{Ra}_{\mathrm{crit}} = \{16.4, 24.7, 41.0\}$ for the three values of E that we use. In addition to a suite of simulations with homogeneous boundaries at both the top and bottom of the shell we carried out simulations in which we imposed one of two patterns of CMB heat flux heterogeneity, one derived from seismic tomography[30] and a hemispheric pattern that could represent the configuration of mantle flow during times of super-continent formation (for the hemispheric pattern q_{min} is located under Null Island). Here we include six additional simulations with the hemispheric boundary forcing and $E = 10^{-6}$.

Brunt-Väisälä frequency The frequency of oscillation of a radially displaced parcel of fluid within a fluid layer having stable density stratification ($\partial\rho/\partial r < 0$) is known as the buoyancy frequency or Brunt-Väisälä frequency and is defined by

$$N = \sqrt{-\frac{g}{\rho_0}\frac{\partial\rho}{\partial r}}. \tag{5}$$

If the density anomalies arise due to purely thermal effects then

$$N = \sqrt{g\alpha \frac{\partial T}{\partial r}}. \tag{6}$$

We choose to non-dimensionalise N by 2Ω, in combination with our temperature and distance scalings this gives

$$\frac{N}{2\Omega} = \sqrt{\frac{g\alpha\beta}{4\Omega^2 L^2}\frac{\partial T^\star}{\partial r^\star}} = \sqrt{\frac{\widetilde{Ra}E}{Pr}\frac{\partial T^\star}{\partial r^\star}}. \tag{7}$$

The steepest temperature gradient in the model corresponds to the maximum buoyancy frequency and we expect that the steepest gradient near the top of the core is close to that set by q_{min} of the imposed CMB heat flux. For a simple pattern of heat flux heterogeneity we would have $q_{\mathrm{ave}} = (q_{\mathrm{max}} + q_{\mathrm{min}})/2$, which combines with our definition of $q^\star$ to gives

$$q_{\mathrm{min}} = -\left(\frac{q^\star - 2}{2}\right) q_{\mathrm{ave}}. \tag{8}$$

From the definition of our boundary conditions $q_{\mathrm{ave}} = k\beta/r_{\mathrm{o}}^2$ and thus we expect

$$\left.\frac{N}{2\Omega}\right|_{\mathrm{max}} \approx \left(\frac{1}{r_{\mathrm{o}}^\star}\right)\sqrt{\frac{\widetilde{Ra}E}{Pr}\left(\frac{q^\star - 2}{2}\right)}. \tag{9}$$

Parameter regime in comparison to Earth's core. The pattern and amplitude of CMB heat flux variations are hard to estimate because they must be inferred from seismic tomography accounting for possible compositional effects and phase changes in the lower mantle. Nevertheless, several studies[25,31,32] have found a minimum heat flux of $q_{\mathrm{min}} \approx 0$ mW m^{-2}, while the maximum heat flux q_{max} could rise above 200 mW m^{-2}. The adiabatic gradient at the CMB $\mathrm{d}T_{\mathrm{a}}/\mathrm{d}r = g\gamma T/\phi \approx -0.875 \pm 0.125$ K km^{-1} with the seismic parameter ϕ and gravity g taken from PREM[33] and the Grüneisen parameter $\gamma = 1.3 - 1.5$ spanning the available estimates[34]. Using low[35] and high[6] thermal conductivity values gives $q_{\rm a} = -k\partial T_a/\partial r = 30 - 90$ mW m^{-2} and therefore hot regions of the lower mantle will result in a subadiabatic heat flux across the CMB. The relative strength of CMB anomalies is often measured by the parameter $q^\star = (q_{\rm max} - q_{\rm min})/(q - q_{\rm a})$, which can take either sign given estimates[5] of $q = 30 - 110$ mW m^{-2}. Here we are interested in the case $q^\star > 0$, as $q^\star$ of at least $O(1)$ is expected within the Earth[25] and it could be significantly greater (indeed $q^\star$ is unbounded as $q \to q_{\rm a}$), in such cases thermal boundary forcing should exert a significant influence on core convection[36].

The other control parameters of our numerical model, E and $\widetilde{Ra}$, primarily reflect a force balance between rotation, viscosity, and buoyancy. The parameter regime appropriate for Earth is at lower E and higher Ra than numerical simulations can attain[37]. If turbulent values of the diffusion coefficients are appropriate for modelling observable core dynamics then $E = 10^{-9}$ for Earth, whereas molecular values of the diffusion coefficients lead to $E = 10^{-15}$. Determination of the Rayleigh number for Earth relies on the poorly known (superadiabatic) heat flux through the CMB, but is likely very large; using 1 TW and reasonable estimates for the other core properties[13] gives $\widetilde{Ra} = 10^{12}$. Consideration based on the force balance between inertia, viscosity, and rotation suggests use of the Reynolds number, $Re = UD/\nu$, and Rossby number, $Ro = U/2\Omega D = ReE$, where U and D are characteristic velocity and and length scales of the flow. In our simulations Re is $O(10^1 - 10^3)$, compared to estimates[38] for Earth's core of $O(10^8)$. In our simulations Ro is $O(10^{-4} - 10^{-1})$, compared to estimates[38] for Earth's core of $O(10^{-7})$.

Dynamically supported lateral temperature variations In a fully convecting core an adiabatic temperature gradient $(\mathrm{d}T_{\rm a}/\mathrm{d}r)$ will extend from the ICB to the CMB, except for within thin boundary layers. Within a regional inversion layer a shallower conductive profile $(\mathrm{d}T_\mathrm{c}/\mathrm{d}r)$ will exist. The temperature difference at the CMB between a fully convecting region and the top of a regional inversion layer of thickness h will be approximately

$$\delta T \approx h\left(\mathrm{d}T_\mathrm{a}/\mathrm{d}r - \mathrm{d}T_\mathrm{c}/\mathrm{d}r\right). \tag{10}$$

If we estimate the conductive temperature gradient throughout the inversion layer from the minimum CMB heat flux, then

$$\mathrm{d}T_\mathrm{c}/\mathrm{d}r = -q_\mathrm{min}/k \tag{11}$$

where k is the thermal conductivity of the core. The value of q_min is mathematically related to both the amplitude of heat flux heterogeneity ($q^\star$) and the mean heat flux through the CMB ($q_\mathrm{ave} = Q/4\pi r_\mathrm{o}^2$), both of which are uncertain for the Earth. The thickness of the thermal inversion layers arises dynamically in our model and thus relies on the imposed CMB heat flux; nevertheless in supplementary figure 5 we assume a fixed value of $h = 250$ km for all cases, along with a thermal conductivity $k = 100$ W m^{-1} K^{-1}. The resultant temperature difference between the regional inversion layers and the fully convecting bulk of the core can be on the order of 10's to 100's of kelvin (supplementary figure 5).

Seismic evidence Several seismic studies have studied the velocity structure of the Earths outermost core[2,3,12,39–41,44]. These studies use travel times of the multiple CMB underside reflections *SmKS*, with m indicating the number of P-wave legs in the outer core, corresponding to $m-1$ CMB underside reflections. Phases with lower values of m turn more deeply within the core and differential travel times of phase pairs, e.g. *S3KS−S2KS* (dt^{3-2}), *S4KS−S3KS* (dt^{4-3}), and *S5KS−S3KS* (dt^{5-3}), are used to develop velocity profiles of the top few hundred kilometres of the outer core.

Evidence for a layered outer core has been found in several studies (for a review see [2]), whereas other studies do not find evidence for a global stable layer[12].

Here we make use of selected results from a recent[3] published dataset; in total we have assembled 58 observations with both well defined source and receiver locations and differential travel time measurements. Where necessary we use estimated locations of the centre points of large scale seismic networks as receiver location. The portion of the paths within the outer core and the differential travel time residuals of the resultant data set are shown in supplementary figure 6, each panel corresponds to a different phase pair. Background colour in supplementary figure 6a shows P-wave velocity variation of tomographic model LLNL-G3D[42]. Coverage of the globe is fairly sparse and due to long path lengths in the core it is unclear how a stably stratified layer will be sampled by the *SmKS* travel time residuals.

As a simple indicator of whether a given path might be sampling a stratified or convecting region we classify the mantle above the core paths as slow or fast based on the velocities of the lowermost mantle above the two *SKKS* turning points; the values of seismic velocity at those locations in tomographic model LLNL-G3D are compared to that of the AK135[43] background. Supplementary figure 7 shows the differential travel times separated into paths under fast and slow mantle. With the presently available data it is not possible to distinguish between a global layer and regional inversion at the top of the core. Future results from regional seismic arrays may provide the necessary seismic data, with lower travel times uncertainties and greater geographic coverage (particularly for dt^{4-3} and dt^{5-3}), required to detect the proposed regional structure at the top of the outer core. Such investigations will also require analysis of 3D numerical wavepropagation models that incorporate such structures in addition to LLVP's and other lower mantle heterogeneity in order to develop a more detailed understanding of how *SmKS* phases sample core regional inversion layers.

1. Lay, T. & Young, C. J. The Stably-Stratified Outermost Core Revisited. *Geophysical Research Letters* **17**, 2001–2004 (1990).

2. Helffrich, G. & Kaneshima, S. Outer-core compositional stratification from observed core wave speed profiles. *Nature* **468**, 807–810 (2010).

3. Kaneshima, S. Array analyses of SmKS waves and the stratification of Earth's outermost core. *Physics of the Earth and Planetary Interiors* **in press**, 1–13 (2017).

4. Buffett, B. Geomagnetic fluctuations reveal stable stratification at the top of the Earth's core. *Nature* **507**, 484–487 (2014).

5. Nimmo, F. Energetics of the Core. In Olson, P. (ed.) *Core Dynamics*, 27–55 (Elsevier, Amsterdam, 2015).

6. Davies, C., Pozzo, M., Gubbins, D. & Alfè, D. Constraints from material properties on the dynamics and evolution of Earth's core. *Nature Geoscience* **8**, 678–685 (2015).

7. Lister, J. R. & Buffett, B. A. Stratification of the outer core at the core-mantle boundary. *Physics of the Earth and Planetary Interiors* **105**, 5–19 (1998).

8. Buffett, B. A. & Seagle, C. T. Stratification of the top of the core due to chemical interactions with the mantle. *Journal of Geophysical Research* **115**, B04407 (2010).

9. Gubbins, D. & Davies, C. J. The stratified layer at the core-mantle boundary caused by barodiffusion of oxygen, sulphur and silicon. *Physics of the Earth and Planetary Interiors* **215**, 21–28 (2013).

10. Olsen, N. *et al.* The CHAOS-4 geomagnetic field model. *Geophysical Journal International* **197**, 815–827 (2014).

11. Amit, H. Can downwelling at the top of the Earth's core be detected in the geomagnetic secular variation? *Physics of the Earth and Planetary Interiors* **229**, 110–121 (2014).

12. Alexandrakis, C. & Eaton, D. W. Precise seismic-wave velocity atop Earth's core: No evidence for outer-core stratification. *Physics of the Earth and Planetary Interiors* **180**, 59–65 (2010).

13. Jones, C. A. Thermal and Compositional Convection in the Outer Core. In Olson, P. (ed.) *Core Dynamics*, 115–159 (Elsevier, Amsterdam, 2015).

14. Braginsky, S. I. Dynamics of the stably stratified ocean at the top of the core. *Physics of the Earth and Planetary Interiors* **111**, 21–34 (1999).

15. Lesur, V., Whaler, K. & Wardinski, I. Are geomagnetic data consistent with stably stratified flow at the core-mantle boundary? *Geophysical Journal International* **201**, 929–946 (2015).

16. Gubbins, D. Geomagnetic constraints on stratification at the top of Earth's core. *Earth, Planets and Space* **59**, 661–664 (2007).

17. Gubbins, D., Alfè, D., Davies, C. & Pozzo, M. On core convection and the geodynamo: Effects of high electrical and thermal conductivity. *Physics of the Earth and Planetary Interiors* **247**, 56–64 (2015).

18. Landeau, M., Olson, P., Deguen, R. & Hirsh, B. H. Core merging and stratification following giant impact. *Nature Geoscience* **9**, 786–789 (2016).

19. Jacobson, S. A., Rubie, D. C., Hernlund, J., Morbidelli, A. & Nakajima, M. Formation, stratification, and mixing of the cores of Earth and Venus. *Earth and Planetary Science Letters* **474**, 375–386 (2017).

20. Olson, P. Thermal interaction of the core and mantle. In *Earth's Core and Lower Mantle*, 1–38 (Taylor & Francis, New York, 2003).

21. Mound, J. E. & Davies, C. J. Heat transfer in rapidly rotating convection with heterogeneous thermal boundary conditions. *Journal of Fluid Mechanics* **828**, 601–629 (2017).

22. Davies, C. J., Gubbins, D. & Jimack, P. K. Convection in a rapidly rotating spherical shell with an imposed laterally varying thermal boundary condition. *Journal of Fluid Mechanics* **641**, 335–358 (2009).

23. Dietrich, W., Hori, K. & Wicht, J. Core flows and heat transfer induced by inhomogeneous cooling with sub- and supercritical convection. *Physics of the Earth and Planetary Interiors* **251**, 36–51 (2016).

24. Olson, P., Landeau, M. & Reynolds, E. Dynamo tests for stratification below the core-mantle boundary. *Physics of the Earth and Planetary Interiors* **271**, 1–18 (2017).

25. Stackhouse, S., Stixrude, L. & Karki, B. B. First-principles calculations of the lattice thermal conductivity of the lower mantle. *Earth and Planetary Science Letters* **427**, 11–17 (2015).

26. Roberts, P. H. & Aurnou, J. M. On the theory of core-mantle coupling. *Geophysical & Astrophysical Fluid Dynamics* **106**, 157–230 (2012).

27. Sahoo, S., Sreenivasan, B. & Amit, H. Dynamos driven by weak thermal convection and heterogeneous outer boundary heat flux. *Physics of the Earth and Planetary Interiors* **250**, 35–45 (2016).

28. Finlay, C. C., Olsen, N., Kotsiaros, S., Gillet, N. & Tøffner-Clausen, L. Recent geomagnetic secular variation from Swarm and ground observatories as estimated in the CHAOS-6 geomagnetic field model. *Earth, Planets and Space* **68**, 112 (2016).

29. Willis, A. P., Sreenivasan, B. & Gubbins, D. Thermal core–mantle interaction: Exploring regimes for 'locked' dynamo action. *Physics of the Earth and Planetary Interiors* **165**, 83–92 (2007).

30. Masters, G., Johnson, S., Laske, G. & Bolton, H. A shear-velocity model of the mantle. *Philosophical Transactions of the Royal Society A: Mathematical, Physical and Engineering Sciences* **354**, 1385–1411 (1996).

31. Nakagawa, T. & Tackley, P. J. Lateral variations in CMB heat flux and deep mantle seismic velocity caused by a thermal–chemical-phase boundary layer in 3D spherical convection. *Earth and Planetary Science Letters* **271**, 348–358 (2008).

32. Olson, P., Deguen, R., Rudolph, M. L. & Zhong, S. Core evolution driven by mantle global circulation. *Physics of the Earth and Planetary Interiors* **243**, 44–55 (2015).

33. Dziewonski, A. M. & Anderson, D. L. Preliminary reference Earth model. *Physics of the Earth and Planetary Interiors* **25**, 297–356 (1981).

34. Ichikawa, H., Tsuchiya, T. & Tange, Y. The P-V-T equation of state and thermodynamic properties of liquid iron. *Journal of Geophysical Research* **119**, 240–252 (2014).

35. Konôpková, Z., McWilliams, R. S., Gómez-Pérez, N. & Goncharov, A. F. Direct measurement of thermal conductivity in solid iron at planetary core conditions . *Nature* **534**, 99–101 (2016).

36. Sumita, I. & Olson, P. Rotating thermal convection experiments in a hemispherical shell with heterogeneous boundary heat flux: Implications for the Earth's core. *Journal of Geophysical Research* **107**, 2169 (2002).

37. Aurnou, J. M. *et al.* Rotating convective turbulence in Earth and planetary cores. *Physics of the Earth and Planetary Interiors* **246**, 52–71 (2015).

38. Olson, P. Core Dynamics: An Introduction and Overview. In *Core Dynamics*, 1–25 (Elsevier B.V., 2015).

39. Kaneshima, S. & Helffrich, G. Vp structure of the outermost core derived from analysing large-scale array data of SmKS waves. *Geophysical Journal International* **193**, 1537–1555 (2013).

40. Eaton, D. W. & Kendall, J.-M. Improving seismic resolution of outermost core structure by multichannel analysis and deconvolution of broadband SmKS phases. *Physics of the Earth and Planetary Interiors* **155**, 104–119 (2006).

41. Kaneshima, S. & Matsuzawa, T. Stratification of earth's outermost core inferred from SmKS array data. *Progress in Earth and Planetary Science* **2**, 15 (2015).

42. Simmons, N. A., Myers, S. C., Johannesson, G. & Matzel, E. LLNL-G3Dv3: Global P wave tomography model for improved regional and teleseismic travel time prediction. *Journal of Geophysical Research* **117**, B10302 (2012).

43. Kennett, B. L. N., Engdahl, E. R. & Buland, R. Constraints on seismic velocities in the Earth from traveltimes. *Geophysical Journal International* **122**, 108–124 (1995).

44. Tang, V., Zhao, L. & Hung, S.-H. Seismological evidence for a non-monotonic velocity gradient in the topmost outer core. *Scientific Reports* **5**, 8613 (2015).

45. Childs, H. *et al.* VisIt: An end-user tool for visualizing and analyzing very large data. In Bethel, E. W., Childs, H. & Hansen, C. (eds.) *High Performance Visualization*, 357–372 (Chapman and Hall, 2012).

46. Hunter, J. D. Matplotlib: A 2D graphics environment. *Computing in Science and Engineering* **9**, 90–95 (2007).

47. Waskom, M. *et al.* mwaskom/seaborn: v0.8.0 (2017).

Supplementary Information ...

Figure 1: Thermal structure in a simulation with a tomographic pattern of CMB heat flux. Left: Green isovolumes denote regions of positive $\mathrm{d}T/\mathrm{d}r$ in the time-average for the simulation with $q^\star = 5.0$, $E = 10^{-6}$, and $\widetilde{Ra} = 1.8 \times 10^4$. Equatorial slice shows the temperature field relative to the average throughout the core for one point in time. Right: Time-averaged profiles of T (top) and $\mathrm{d}T/\mathrm{d}r$ (bottom) in the top half of the outer core for this simulation; dashed orange line is the spherical average, dotted blue lines are individual profiles from locations on the equator ($\theta = \pi/2$), with east longitude $\phi = 0$, $\pi/2$, π, $3\pi/2$. The green solid line is the spherical average from a simulation with homogeneous boundary conditions, but otherwise run at identical parameters. Temperature has been non-dimensionalised as described in the methods section.

Acknowledgements CJD is supported by a Natural Environment Research Council Independent Research Fellowship (NE/L011328/1). Figures were produced using VisIt[45], Matplotlib[46] and seaborn[47].

Competing Interests The authors declare that they have no competing financial interests.

Author Information Correspondence and requests for materials should be addressed to Jon Mound. (email: j.e.mound@leeds.ac.uk).

Author Contributions All discussed and developed the central ideas and contributed to the writing of the manuscript. JM and CD carried out the numerical modelling and analysis. SR analysed the seismic data.

Figure 2: Regional stratification characteristics for all simulations as a function of the combination of parameters expected to control stratification strength. Thickness (top) and maximum Brunt-Väisälä frequency (bottom) of the regional inversion layer under Africa (left) and the Pacific (right). Symbol shape: hemispheric (hexagons) or tomographic (triangles) CMB heat-flux patterns. Symbol colour: $E = 10^{-6}$ (lavender), 10^{-5} (green), 10^{-4} (brick). Symbol size: $q^\star = 2.3$ (small), 5.0 (large).

Figure 3: Regional profiles of time-averaged temperature gradient in the top half of the core. The profiles are taken at $\theta = \pi/2$ and $\phi = 0$ (left) or $\phi = \pi$ (right) from a simulation with a tomographic CMB heat-flux pattern, $q^\star = 5.0$, and $E = 10^{-4}$ (top), 10^{-5} (middle), or 10^{-6} (bottom). Colour of the lines indicates the super-criticality of the modified Rayleigh number from 10 times critical (light) to 1000 times critical (dark). Temperature has been non-dimensionalised as described in the methods section.

Figure 4: Flow near the top of the core for the simulation in figure 1. Time average of the radial velocity (top), azimuthal velocity (bottom), and contours of $\mathrm{d}T/\mathrm{d}r = 0$ (green) at a radius of 3367 km. The averaging was done over 37 advection times. The flow velocity is non-dimensionalised as described in the methods section.

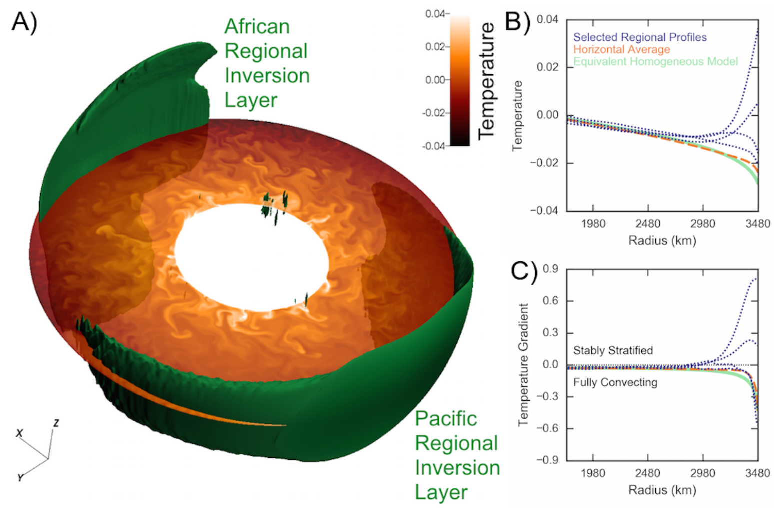
A)
African
Regional
Inversion
Layer
Temperature
0.04
0.02
0.00
-0.02
-0.04
Pacific
Regional
Inversion
Layer
X
Z
Y
B)
Selected Regional Profiles
Horizontal Average
Equivalent Homogeneous Model
Temperature
0.04
0.02
0.00
−0.02
−0.04
1980
2480
2980
3480
Radius (km)
C)
Temperature Gradient
0.9
0.6
0.3
0.0
−0.3
−0.6
−0.9
Stably Stratified
Fully Convecting
1980
2480
2980
3480
Radius (km)

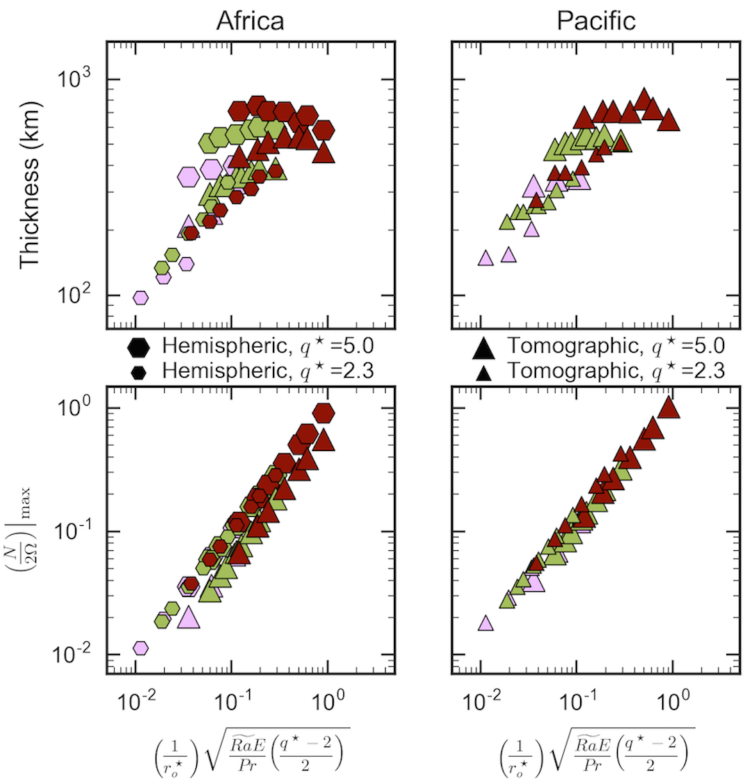

Africa
Pacific
Thickness (km)
10^3
10^2
Hemispheric, $q^\star$ =5.0
Hemispheric, $q^\star$ =2.3
Tomographic, $q^\star$ =5.0
Tomographic, $q^\star$ =2.3
$\left(\frac{N}{2\Omega}\right)\Big|_{\max}$
10^0
10^{-1}
10^{-2}
10^{-2}
10^{-1}
10^0
$\left(\frac{1}{r_o^\star}\right)\sqrt{\frac{\widetilde{Ra}E}{Pr}\left(\frac{q^\star-2}{2}\right)}$

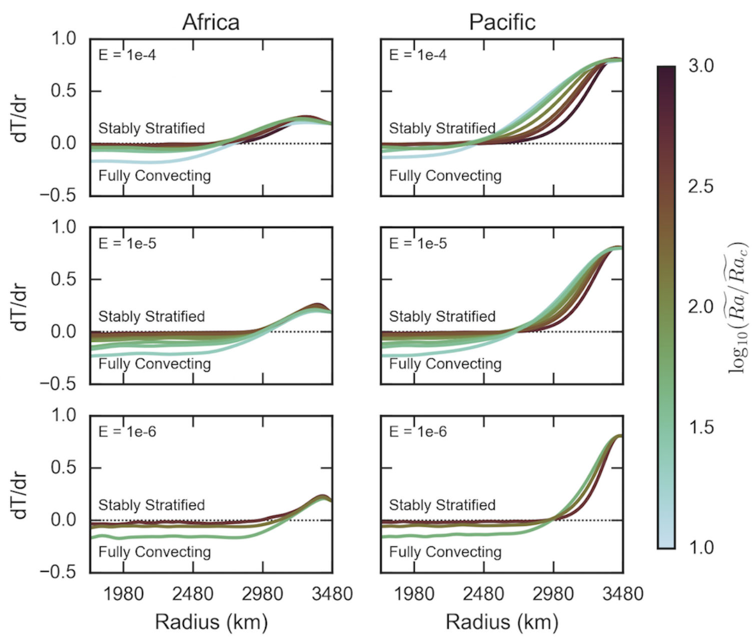

Africa
Pacific
E = 1e-4
E = 1e-5
E = 1e-6
Stably Stratified
Fully Convecting
dT/dr
Radius (km)
1980
2480
2980
3480
1.0
0.5
0.0
−0.5
3.0
2.5
2.0
1.5
$\log_{10}(\widetilde{Ra}/\widetilde{Ra_c})$

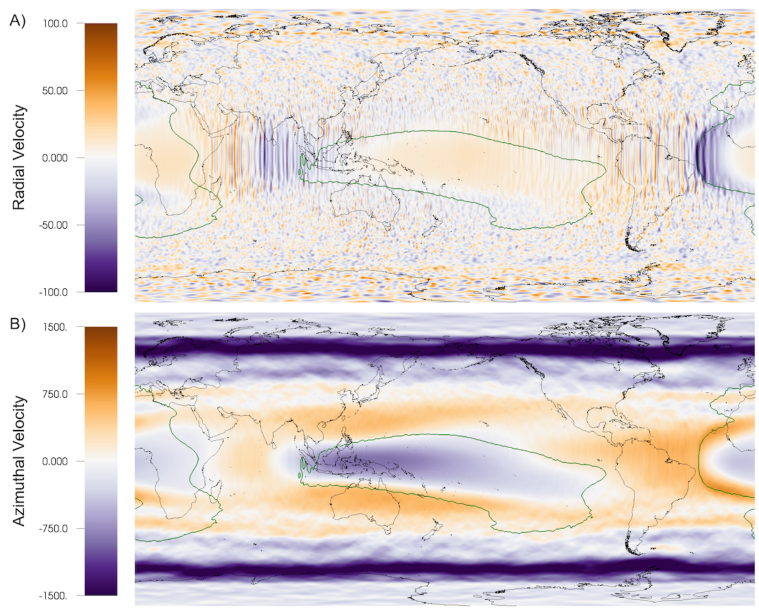
A)
100.0
50.00
0.000
-50.00
-100.0
Radial Velocity
B)
1500.
750.0
0.000
-750.0
-1500.
Azimuthal Velocity

Supplementary Information for "The Apparent Stratification at the Top of Earth's Liquid Core"

Jon Mound[1], Chris Davies[1], Sebastian Rost[1] & Jon Aurnou[2]

[1]*School of Earth and Environment, University of Leeds, Leeds LS2 9JT, UK*

[2]*Department of Earth and Space Sciences, University of California, Los Angeles, California 90095-1567, USA.*

Figure 1: Thermal structure in a simulation with a hemispheric pattern of CMB heat flux. Left: Green isovolumes denote regions of positive $\mathrm{d}T/\mathrm{d}r$ in the time-average for a simulation with $q^{\star} = 5.0$, $E = 10^{-6}$, and $\widetilde{Ra} = 1.8 \times 10^{4}$. Equatorial slice shows the temperature field relative to the average throughout the core for one point in time. Right: Time-averaged profiles of T (top) and $\mathrm{d}T/\mathrm{d}r$ (bottom) in the top half of the outer core for this simulation; dashed orange line is the spherical average, dotted blue lines are individual profiles from locations with $\theta = \pi/2$ and $\phi = 0$, $\pi/2$, π, $3\pi/2$. The green solid line is the spherical average from a simulation with homogeneous boundary conditions, but otherwise run at identical parameters. Temperature has been non-dimensionalised as described in the methods section.

Figure 2: Global profiles of time-averaged temperature gradient in the top half of the core for simulations with a tomographic CMB heat-flux pattern. Horizontally averaged profiles taken from simulations with $q^{\star} = 2.3$ (left) or 5.0 (right), and $E = 10^{-4}$ (top), 10^{-5} (middle), or 10^{-6} (bottom). Colour of the lines indicates the super-criticality of the modified Rayleigh number from 10 times critical (light) to 1000 times critical (dark). Temperature has been non-dimensionalised as described in the methods section.

Figure 3: Global profiles of time-averaged temperature gradient in the top half of the core for simulations with a hemispheric CMB heat-flux pattern. Horizontally averaged profiles taken from simulations with $q^{\star} = 2.3$ (left) or 5.0 (right), and $E = 10^{-4}$ (top), 10^{-5} (middle), or 10^{-6} (bottom). Colour of the lines indicates the super-criticality of the modified Rayleigh number from 10 times critical (light) to 1000 times critical (dark). Temperature has been non-dimensionalised as described in the methods section.

Figure 4: Apparent global stratification characteristics versus super-criticality for simulations that produce depth ranges with horizontally averaged $\partial T/\partial r > 0$. Thickness (top) and Brunt-Väisälä frequency (bottom) of the horizontally averaged structure. Symbol shape: hemispheric (hexagons) or tomographic (triangles) CMB heat-flux patterns. Symbol colour: $E = 10^{-5}$ (green), 10^{-4} (brick). All of these models have $q^{\star} = 5.0$.

Figure 5: Excess temperature of the stratified regions. Contours of excess temperature (in kelvin) at the top of the core as a function of the total CMB heat flow, Q, and the strength of heterogeneity, $q^{\star}$. This example considers a layer thickness $h = 250$ km, total adiabatic heat flow $Q_{\mathrm{ad}} = 9$ TW, and thermal conductivity $k = 100$ W m^{-1} K^{-1}.

Figure 6: Sources (stars), network centres (triangles) and paths of *SmKS* in the outer core (lines). The *SKKS* CMB reflection points are shown as coloured circles, the colour representing the differential travel time residual for each *SmKS* combination. (A) Measurements for dt^{3-2} (*S3KS*−*S2KS*). Background colour shows P-wave velocity variation of model LLNL-G3D. (B) Measurements for dt^{4-3} (*S4KS*−*S3KS*), (C) Measurements for dt^{5-3} (*S5KS*−*S3KS*).

Figure 7: Differential travel times of each phase pair extracted from Kaneshima (2017) divided into fast and slow regions based on the average velocity of the lowermost mantle above the two SKKS turning points in the outer core. Mantle velocity base on LLNL-G3D relative to AK135. Average mantle velocity is given by symbol colour. Datapoint uncertainties as defined in Kaneshima (2017) are shown.

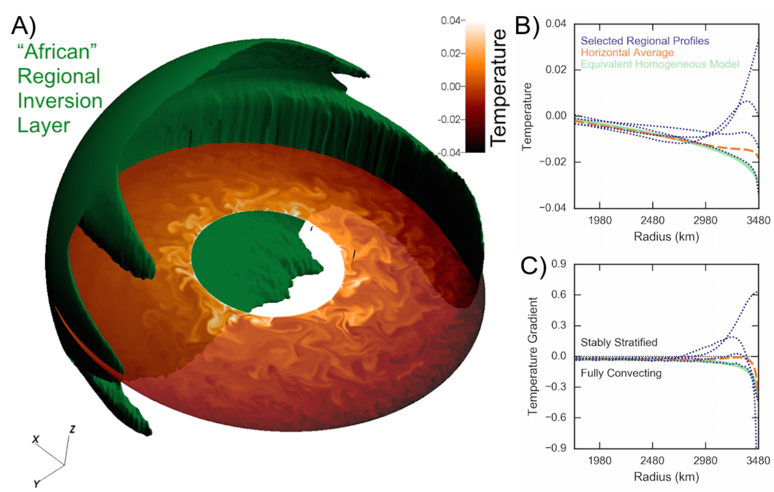
A)
"African"
Regional
Inversion
Layer
0.04
0.02
0.00
-0.02
-0.04
Temperature
X
Z
Y
B)
Selected Regional Profiles
Horizontal Average
Equivalent Homogeneous Model
Temperature
0.04
0.02
0.00
−0.02
−0.04
1980
2480
2980
3480
Radius (km)
C)
0.9
0.6
0.3
0.0
−0.3
−0.6
−0.9
Temperature Gradient
Stably Stratified
Fully Convecting
1980
2480
2980
3480
Radius (km)

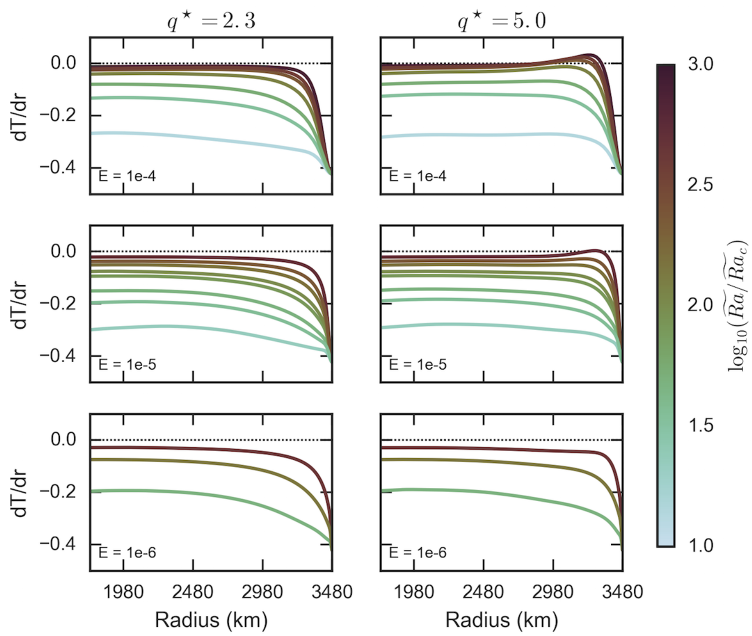

$q^\star = 2.3$
$q^\star = 5.0$
dT/dr
0.0
−0.2
−0.4
E = 1e-4
E = 1e-5
E = 1e-6
1980
2480
2980
3480
Radius (km)
$\log_{10}(\widetilde{Ra}/\widetilde{Ra}_c)$
1.0
1.5
2.0
2.5
3.0

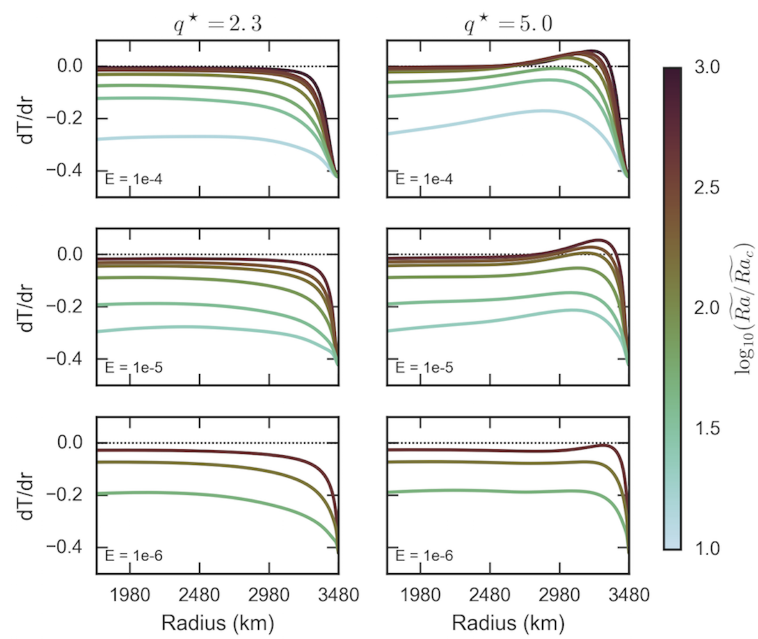

$q^\star = 2.3$
$q^\star = 5.0$
dT/dr
0.0
−0.2
−0.4
E = 1e-4
E = 1e-5
E = 1e-6
1980
2480
2980
3480
Radius (km)
3.0
2.5
2.0
1.5
1.0
$\log_{10}(\widetilde{Ra}/\widetilde{Ra}_c)$

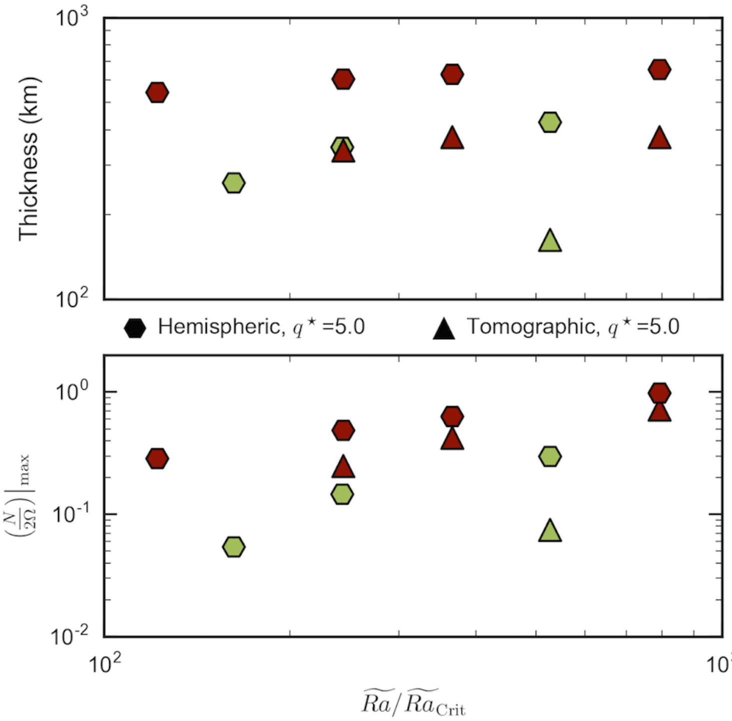

Thickness (km)
10^3
10^2
Hemispheric, $q^\star$ =5.0
Tomographic, $q^\star$ =5.0
$\left(\frac{N}{2\Omega}\right)\Big|_{\max}$
10^0
10^-1
10^-2
10^2
10^3
$\widetilde{Ra}/\widetilde{Ra}_{\mathrm{Crit}}$

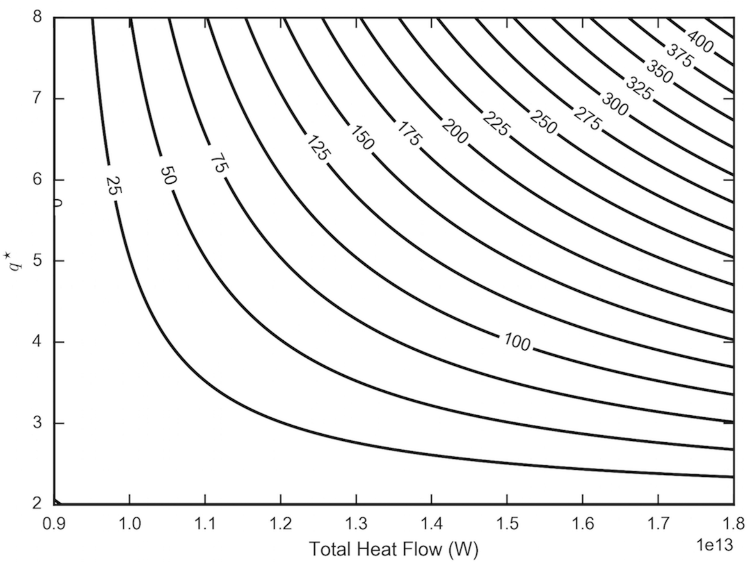

8
7
6
5
4
3
2
q*
0.9
1.0
1.1
1.2
1.3
1.4
1.5
1.6
1.7
1.8
1e13
Total Heat Flow (W)
25
50
75
100
125
150
175
200
225
250
275
300
325
350
375
400

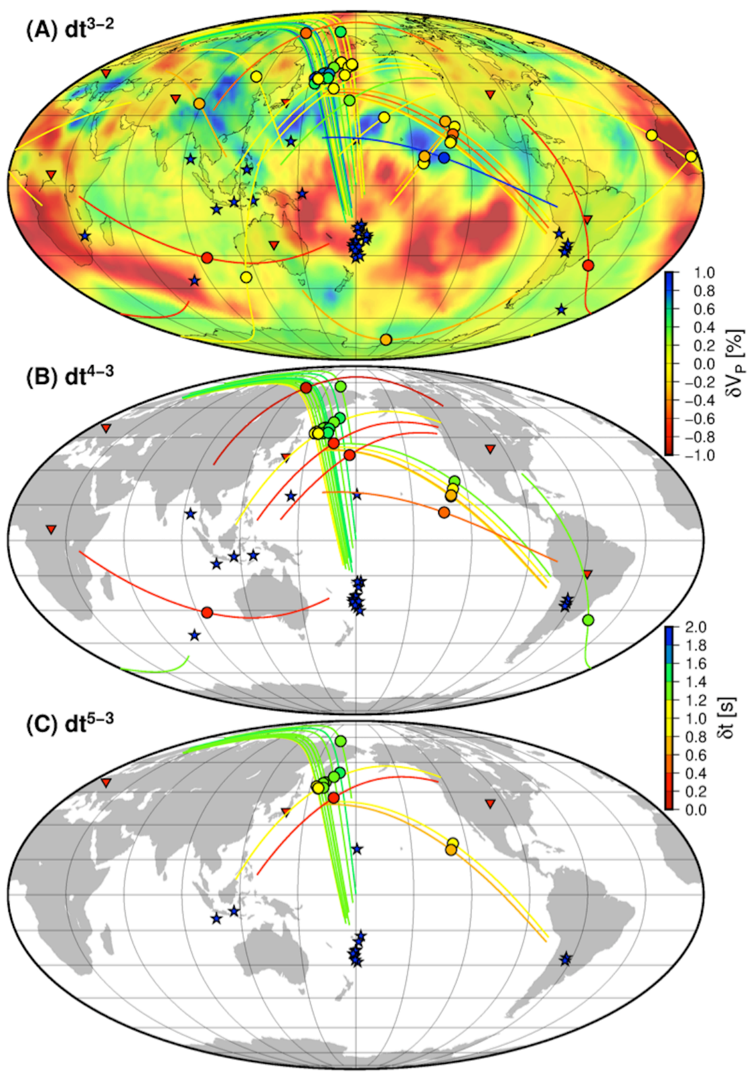
(A) dt$^{3-2}$
(B) dt$^{4-3}$
(C) dt$^{5-3}$
δV_P [%]
1.0
0.8
0.6
0.4
0.2
0.0
−0.2
−0.4
−0.6
−0.8
−1.0
δt [s]
2.0
1.8
1.6
1.4
1.2
1.0
0.8
0.6
0.4
0.2
0.0

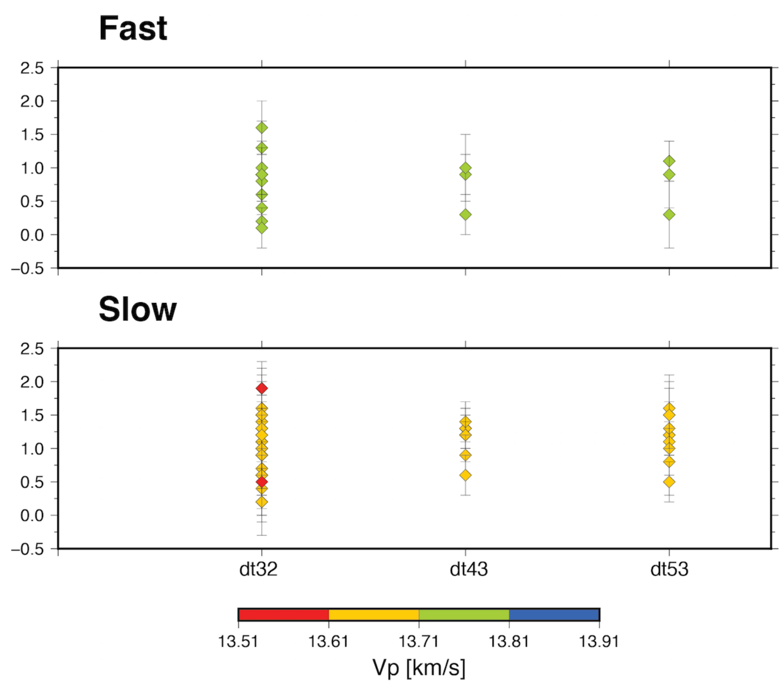
Fast
Slow
2.5
2.0
1.5
1.0
0.5
0.0
−0.5
dt32
dt43
dt53
13.51
13.61
13.71
13.81
13.91
Vp [km/s]